Serb. Astron. J. № 207 (2023), 9 - 19
DOI: https://doi.org/10.2298/SAJ2307009V

UDC 524.354–75
Original scientific paper

PROPER MOTION OF CYGNUS LOOP SHOCK FILAMENTS

M. Vučetić[1], N. Milanović[2], D. Urošević[1], J. Raymond[3], D. Onić[1], S. Milošević[1] and N. Petrov[4]

[1] *Department of Astronomy, Faculty of Mathematics, University of Belgrade, Studentski trg 16, 11000 Belgrade, Serbia*

E–mail: *milica.vucetic@matf.bg.ac.rs*

[2] *Max Planck Institute for Solar System Research, Justus-von-Liebig-Weg 3, 37077 Göttingen, Germany*

[3] *Harvard-Smithsonian Center for Astrophysics, 60 Garden Street, Cambridge, MA, 02138, USA*

[4] *Institute of Astronomy and National Astronomical Observatory, Bulgarian Academy of Sciences, Tsarigradsko Shose 72, BG-1784 Sofia, Bulgaria*

(Received: October 22, 2023; Accepted: December 15, 2023)

SUMMARY: We determined the shock speed in the Galactic supernova remnant Cygnus Loop, using the proper motion of its optical filaments and the latest estimate of its distance. The proper motion was measured by comparing Hα images of the remnant observed in two epochs: 1993 (Kitt Peak National Observatory) and 2018/2019 (National Astronomical Observatory Rozhen and Astronomical Station Vidojevica). We derived shock speed for 35 locations along different filaments, which is twice as much as in earlier studies of the north-eastern part of the Cygnus Loop. For the first time, we have measured the shock speed of the radiative filaments in this region. Three of the analyzed locations where we measured the proper motion of filaments are radiative, based on their presence in [SII] images from the second epoch. The other filaments are non-radiative. The speed we obtained for the non-radiative filaments is in the range of 240–650 km s^{-1}, with an estimate for the uncertainty of 70 km s^{-1}. These values are mostly in agreement with previous studies. The radiative filaments have lower speeds of 100–160 ± 70 km s^{-1}, which is in agreement with the assumption that they are older in evolutionary terms. This clear distinction between the speed of the two types of filaments proves that [SII] emission can be used for identifying radiative filaments in supernova remnants.

Key words. ISM: individual (Cygnus Loop) – ISM: supernova remnants – Shock waves

1. INTRODUCTION

The Cygnus Loop is a Galactic supernova remnant (SNR) G74.0-8.5, also known as the Veil Nebula. Recently, its distance was estimated to be 725 ± 15 pc (Fesen et al. 2021), based on the parallaxes of stars available in the Gaia Early Data Release 3. With this result, the uncertainty of the Cygnus Loop distance was reduced to a value comparable to its radius (∼ 18 pc; Fesen et al. 2021). This is significant because the distances to the Galactic SNRs cannot be determined easily. One way to estimate the distance is by taking into account distances to the stars known to be in front or behind the remnant. The ones that are behind can be recognized by absorption in their spectra, caused by the star's radiation passing through the SNR on its way to the observer. The estimated distance to the Cygnus Loop ranged between 440 pc and 1400 pc over the years (see review by Fesen et al. 2018a). With the latest result by Fesen et al. (2021), it eventually came close to the value of 770 pc given by Minkowski (1958) more than 60 years ago.

This middle-aged remnant ($\sim$ 20000 years old) has an apparent diameter of $\sim 3^\circ$ in the sky, and its size and brightness make it suitable for studying smaller structures (filaments) in the remnant. Newest findings suggest that Cygnus Loop's morphology is a consequence of its location in a low-density medium, far from the Galactic plane (b $\approx 8^\circ$). Although being far from Galactic plane, Cygnus Loop encounters interstellar clouds as it expands (Fesen et al. 2018b). The brightest regions observed in the optical domain shape out nearly spherical western and eastern parts of the shell, whose radiation can be described by interaction of the shock wave with the surrounding dust clouds (Hester and Cox 1986).

As the shock front in the SNR decelerates, the downstream region (behind the shock) loses more energy through radiation and cools down. This creates conditions in the downstream region suitable for formation of, for example, forbidden [SII] $\lambda\lambda$ 6716, 6731 emission lines (Raymond 1979, Matonick and Fesen 1997). There, the collisionally excited sulfur ions radiate strongly, typically producing line intensities that compare to Hα as [SII]/H$\alpha > 0.4$. Based on this, it is suggested that the filaments in the remnant that have already entered the radiative phase of the evolution can be recognized through their [SII] emission.

The Cygnus Loop contains both non-radiative and radiative filaments (Hester et al. 1994). Studies of the north-eastern part of the Cygnus Loop so far measured the speed of the non-radiative filaments using different techniques (see Salvesen et al. 2009, Medina et al. 2014, Sankrit et al. 2023). In this paper, for the first time, we determined the speed of the shock wave by measuring the proper motion of both non-radiative and radiative filaments in the Cygnus Loop. The proper motion was measured by comparing the Hα observations from two epochs: 1993 and 2018/2019 (Milanovic et al. 2019). The speed of the filaments was derived using the latest estimate of the remnant's distance, mentioned above. To differentiate between radiative and non-radiative filaments, we observed Cygnus Loop through Hα and [SII] narrowband filters. Radiative filaments of this SNR were recognized as those that are visible in the images taken through narrowband [SII] filter (like in e.g. Vučetić et al. 2015). In this way, we compared the speed of the radiative and non-radiative filaments. We then tested the hypothesis that the radiative filaments should have lower speeds, since they are supposed to be older in evolutionary terms.

The speed of the shocks producing non-radiative filaments is important for other reasons as well. Salvesen et al. (2009) combined the shock speed with the Rankine-Hugoniot shock jump conditions to place upper limits on the fraction of shock energy that goes into the cosmic rays. More recently, Raymond et al. (2023) used the shock speed and jump conditions as one way to determine the electron-ion temperature ratios in shocks.

Optical data used in this paper are described in Section 2, while the method used for the filaments' proper motion measurements is presented in Section 3. Section 4 contains results and discussion. The paper summary is given in Section 5.

2. OBSERVATIONS AND DATA REDUCTION

Shock speed in the Galactic SNR Cygnus Loop was determined using the proper motion of its optical filaments. The proper motion was measured by comparing the Hα images of the remnant observed in two epochs: 1993 and 2018/2019. The speed of each filament was then calculated using the latest estimate for the distance to the object $d = 725 \pm 15$ pc (Fesen et al. 2021).

Data from the Epoch 1 were acquired in 1993[1]. The observations were performed using the Burrell-Schmidt telescope (diameter of 0.9 m) at the National Astronomical Observatory Kitt Peak (KPNO). The data consist of an image taken through a narrowband filter centered around the Hα emission line, with the exposure time of 1500 s. The diameter of the field of view (FOV) is approximately $0\overset{\circ}{.}7$, with a plate scale of $2\overset{''}{.}0268$/px. These data are shown in Fig. 1.

Data from Epoch 2 were acquired during 2018 and 2019 at the National Astronomical Observatory Rozhen (NAO Rozhen) in Bulgaria, and in 2019 at the Astronomical Station Vidojevica (ASV) in Serbia. Observations from Epoch 2 consist of images taken through Hα and [SII] narrowband filters. The Hα images were used for proper motion measurements, while the [SII] images were used only for identification of the radiative filaments.

At the NAO Rozhen, we used their m telescope with a FOV of $5' \times 5'$, and a plate scale of $0\overset{''}{.}176$/px. Seeing conditions ranged from $1\overset{''}{.}2$ to $1\overset{''}{.}8$. In 2018 we observed 8 FOVs (locations marked with squares from A to I in Fig. 1), and in 2019 we observed 3 FOVs (squares K, L, M in Fig. 1). Our aim was to cover as many optical filaments as possible, that were contained in the Epoch 1 data. Each FOV was observed multiple times (5 – 9, depending on FOV) with an exposure time of 300 s. Single exposures were combined to obtain higher signal-to-noise ratio. Narrowband Hα and [SII] filters used from NAO Rozhen are $\sim$30Å wide and are centered at 6572Å and 6719Å, respectively.

Observations from the ASV were done using 1.4 m telescope Milanković. This instrument has a larger FOV of $13' \times 13'$, and a plate scale of $0\overset{''}{.}39$/px. We observed one FOV, its location marked with J in Fig. 1. Seeing conditions ranged from $1''$ to $2''$, and we took 12 images of 300 s through each filter. Narrowband Hα and [SII] filters used from ASV are $\sim$50Å wide, and are centered at 6561Å and 6728Å, respectively.

[1] We received these data in private communication with Prof. Robert A. Fesen (Dartmouth College).

Table 1: Log of observational data: instrument, date of the observations, exposure time $T_{\rm exp}$, size of the FOV, plate scale, used filters. Labels refer to the fields observed in Epoch 2, marked in Fig. 1

Instrument	Date	$T_{\rm exp}$ [s]	FOV	scale [″/px]	filters	labels
			Epoch 1			
KPNO	1993 Aug 16	1500	0°.7	2.0268	Hα	
			Epoch 2			
NAO Rozhen	2018 Sept 12	1500-2700	$5' \times 5'$	0.176	Hα, [SII]	A - I
NAO Rozhen	2019 Oct 1	2400	$5' \times 5'$	0.176	Hα	K, L, M
ASV	2019 Oct 28	3600	$13' \times 13'$	0.39	Hα, [SII]	J

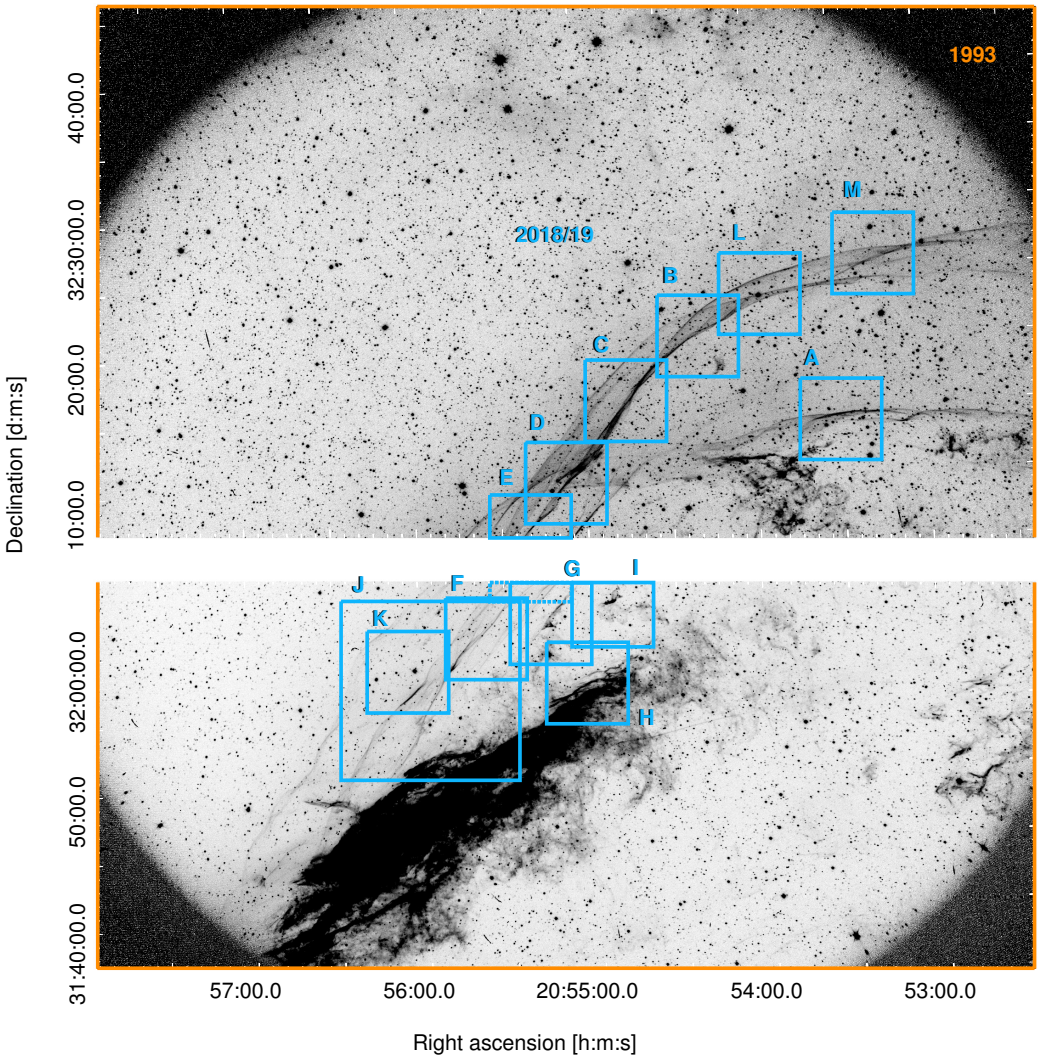

Fig. 1: Context of our observations. The background image represents the Epoch 1 (year 1993) Hα-line image of the northeastern part of the Cygnus Loop. The blue squares mark the fields observed in Epoch 2 (years 2018, 2019), labeled with letters from A to M. Field E is split between the top and the bottom image from Epoch 1, and the dashed blue rectangle marks its bottom part. See Section 2.

Details of observations in both epochs are given in Table 1. We reduced the data from Epoch 2 using standard procedures (bias and flat-field corrections, aligning and combining multiple exposures of the same FOV) in Python language. The data from Epoch 1 we received as already reduced.

3. FILAMENTS' PROPER MOTION MEASUREMENT

To measure the shock speed of the optical filaments, we first linearly interpolated the image from the Epoch 1 to the plate scale of the Epoch 2 images ($2\farcs0268$/px to $0\farcs176$/px or $0\farcs39$/px). Then we aligned Epoch 1 and Epoch 2 images according to the world coordinate system (WCS). For an astrometric solution of the images (setting up the WCS grid and writing the corresponding FITS header keywords), we used the online platform Astrometry[2] (Lang et al. 2010). This web platform performs robust source detection in the input image, than asterisms - sets of four or five stars - are geometrically hashed and compared to the pre-indexed hashes, which are generated by using a combination of Gaia-DR2 and Tycho-2 catalogues.

The next step was selecting suitable regions in both epochs for proper motion measurements. We searched for nearly linear filaments, without too many bright nearby stars, and without other close filaments that would interfere with the measurement. We also chose filaments that are bright enough and stand well above the background level, to make it easier for our routines to recognize the position of the filament.

During measurement process, from each FOV marked in Fig. 1, we selected smaller square subimages (size of $100'' \times 100''$ in most cases), which contained one or more approximately linear filaments. Pairs of subimages at the same location were selected simultaneously from Epochs 1 and 2, according to the WCS. In this way, we isolated a total of 43 filaments, for which we measured the proper motion using the method we discuss below. Some of these filaments were, however, excluded from the analysis after the measurement, for reasons that we will explain in Section 4.

Before further measurements, each filament was rotated to be in a roughly vertical position. This rotation was done to measure the proper motion in the direction of the x-axis in the image. The angle of rotation was estimated by eye for each filament, while the same angle was used for the filament in both epochs. Fig. 2 shows an example of an approximately linear filament, cut from the region B, in Epochs 1 and 2. The filament is shown in its original orientation in the images and is then rotated to make it nearly vertical.

In order to define the position of the filament in the subimages after rotation, we selected slices of the image that enclose the filament motion between the two epochs. These are the same slices in both epochs, marked with dashed rectangles in the second panel in Fig. 2. The rectangles are placed in a way to cross the shock, but omit the areas containing stars, or parts of neighboring filaments. This method ensures that the brightness of the propagating shock dominates its surroundings in the selected slices.

Further on, in each row of pixels along the slice we identified the point with the maximum brightness and used it as the position of the filament in that row. Thus, the position of the filament in each epoch was described by one set of points, where the y-coordinate indicates the rows and the x-coordinate indicates columns of pixels on the slice. These points are over-plotted in the second panel in Fig. 2.

Although we carefully selected slices suitable for measurement of each filament, sometimes the points that obviously belong to the surrounding stars were still caught in the sample. This was especially influenced by the shape of the stars in the Epoch 1 image, which appear larger and smeared due to the lower image quality. This trade-off between placing as large rectangles as possible (to increase the number of measured points) and avoiding stars made the measurement more difficult. Some of these points, which obviously do not belong to the filament, can be seen within the dashed rectangles in Fig. 2.

Apart from the neighboring stars, points that belong to another nearby filament were sometimes caught in the sample, when there are two filaments crossing each other or generally being close in the image. Furthermore, in the case of filaments that were not very bright, the selected points appeared more dispersed than for the brighter filaments. For all these reasons, after selecting the points that represent a filament, we applied a filtering process. To address this, we used an iterative method of sigma-clipping, which we repeated three times. A straight line was fitted to the set of points, in each epoch. After the fitting, the measured points whose x-coordinate (in either of the two epochs) deviated by more than $\pm\, 2\sigma$ from the linear fit were discarded. The points we show in the third panel in Fig. 2 are the final sample points that represent the filament, after the filtering process was applied.

Finally, after rotation and selection of the points that represent the filament in the images, we measured the proper motion of the filament. To this end, we fitted the filament with a vertical regression $x = x(y)$ in each epoch (straight lines in the third and the fourth panel in Fig. 2). Using the images from the two epochs, we calculated the difference between the fitted x-coordinates of the filament in each row. The mean value of the difference was then projected onto the direction perpendicular to the filament (x-axis), and taken as the proper motion of the filament over the time interval between the two epochs.

To estimate the expected value p and the uncertainty Δp of the proper motion, we used a bootstrap re-sampling procedure, where we repeated the above measuring process 10000 times. In each iteration, from the filtered set of points that represent the filament, a new random sample of points was chosen. The sample had always the same number of points as the initial set, with allowed repetition of points.

[2] http://nova.astrometry.net

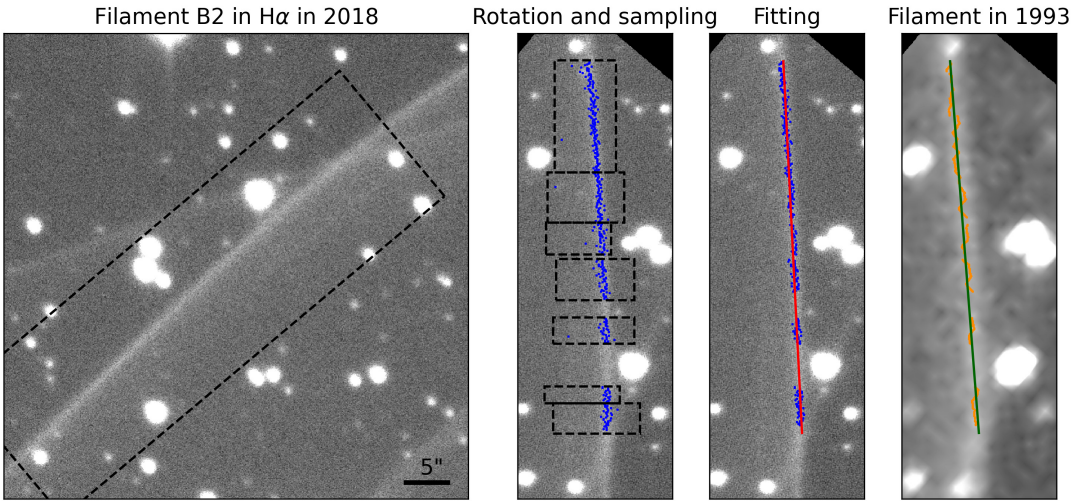

Fig. 2: Illustration of the measurement process for the filament B2. The first panel shows the filament, observed in Epoch 2 in Hα emission. The black rectangle outlines the area shown in the next two panels. In the second panel, the filament is rotated by 130° clockwise, to be nearly vertical. The dashed rectangles show the slices selected for measurement. The points selected to represent the position of the filament (before filtering) are shown in blue. In the third panel, we show the filtered points and the linear fit to the filament (red). The fourth panel shows the same filament when observed in Epoch 1, with the corresponding selected points and the linear fit. See Section 3.

After all the iterations, we obtained a distribution of the measured proper motions, and we took its mean value as the final expected value of p. Since the dispersion of the distribution was always smaller than the pixel size, we used the pixel size ($0\farcs176$ or $0\farcs39$) for the uncertainty Δp.

4. RESULTS AND DISCUSSION

Assuming that the the shock front is moving in the plane of the sky and that the shock speed was constant between the two epochs of our observations, we used the measured proper motion of the filaments to derive their speed. In Table 2 we list the coordinates, the measured proper motion, and the derived speed for 35 locations on different filaments. Only two filaments, all located in our FOV H, were detected in [SII] images, and hence are designated as being in the radiative phase. Fig. 3 shows FOV H and FOV B, to illustrate the difference between radiative and non-radiative filaments. Non-radiative filaments are not visible in [SII] images, while radiative filaments in FOV H are clearly visible. These filaments are the most well-defined filaments in our sample, and we have measured their speed to be in the range of 100–160 $\pm$ 20 km s^{-1}.

We estimated the uncertainty of the proper motion from the boot-strap measurement procedure to $0\farcs2$ – $0\farcs4$. Additional systematic uncertainty arises from astrometric calibration of the images from both epochs. As mentioned in Section 3, the astrometric calibration was made using astrometry.net web-platform. The WCS uncertainty of Epoch 1 is calculated to be $0\farcs4$, while the WCS uncertainty of Epoch 2 is $0\farcs15$. We calculate the total error for proper motion Δp as the sum in quadrature of the measurement procedure error and WCS error of the measurement procedure and WCS error, since they are independent. We calculated the uncertainty for the speed Δv to be 70 km s^{-1} using the uncertainty for the proper motion $\Delta p = 0\farcs6$ and the distance to the remnant of 725 $\pm$ 15 pc (Fesen et al. 2021).

We compared our results to the measurements from earlier works of Salvesen et al. (2009), Medina et al. (2014), and Sankrit et al. (2023), who analyzed similar regions of the Cygnus Loop as we did.

In the work of Salvesen et al. (2009), the speed of 18 non-radiative filaments was measured using a method similar to the one used in this work. The speed of the filaments was determined by comparing images from two different epochs (39.1 years apart). The filaments were also rotated before the measurements, so that they are nearly vertical, and the direction of the shock wave propagation is horizontal. After the rotation, the pixel values were summed up along the vertical direction (columns), for each epoch individually, to obtain an intensity curve along the filament, whose peak should correspond to the brightest part of the shock wave front. Proper motion was then obtained from one-dimensional cross-correlation of the intensity curves in two epochs. In this paper, we have also tried to use a similar one-dimensional cross-correlation method, but it did not work, probably because of a large difference in pixel size between epochs.

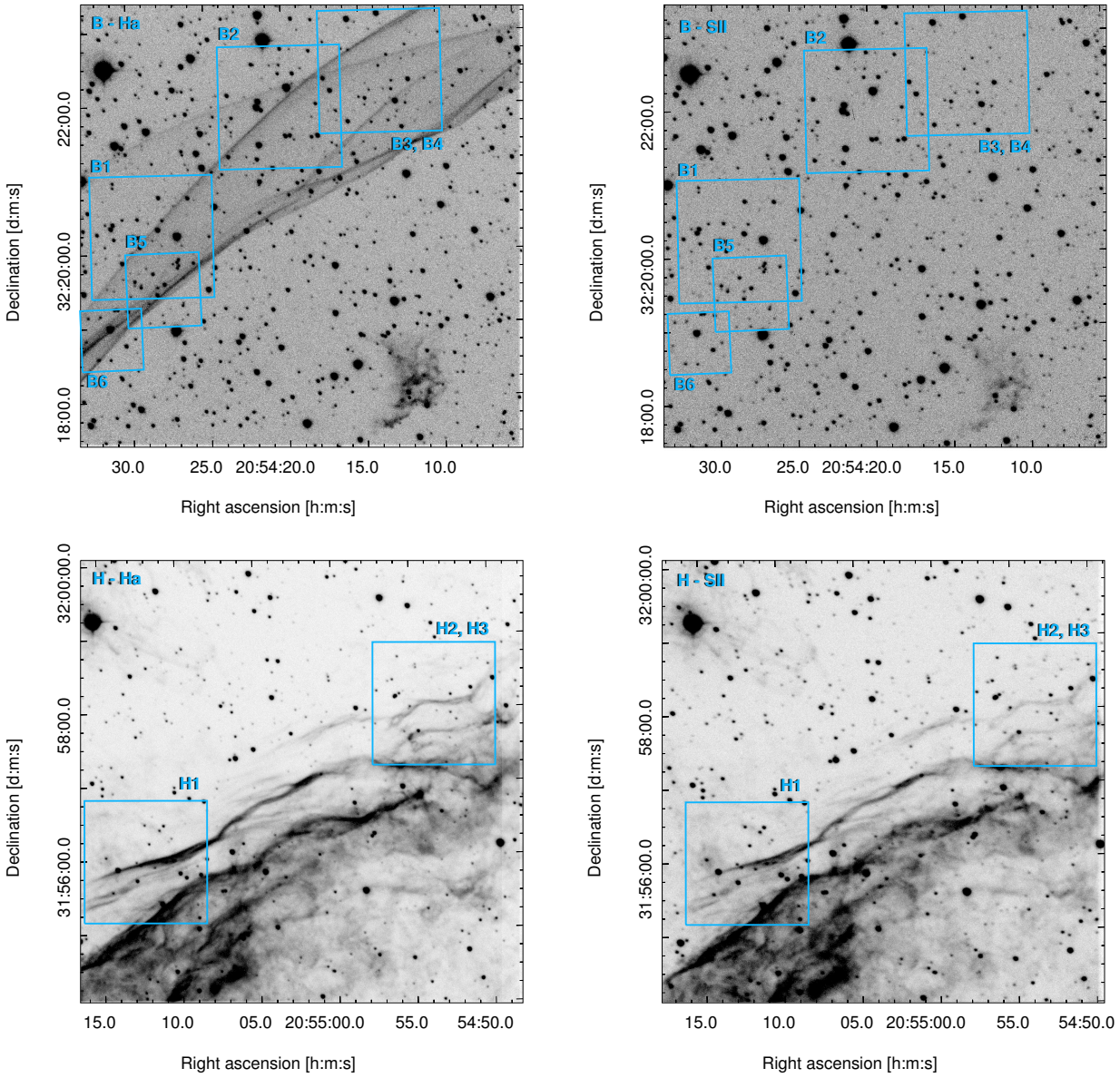

Fig. 3: The top two images show Hα and [SII] images of observed FOV *B*, which contains faster, non-radiative filaments, seen only on the Hα image. The bottom two images show FOV *H*, the only field of view where we see filaments emitting in the [SII] lines, which we assume are in the radiative phase of the SNR evolution. For these filaments, we measure the lowest velocities.

In the work of Medina et al. (2014), the authors performed spectroscopic measurements and obtained: intensity, width, and centroid of the narrow and wide component of the Hα line. The line widths of the broad component represent the post-shock kinetic energy and from shock models (Ghavamian et al. 2001, Chevalier et al. 1980) they estimated shock velocity. They measured 22 different positions in the remnant, located in the non-radiative filaments. To improve the signal-to-noise ratio, some close positions were grouped. After comparing these measurements from spectroscopic observations with the model specified in the paper, the speed of 13 different positions (filaments) was obtained. It is important to note that this method of determining the speed of the filament does not depend on the distance, unlike the method used in Salvesen et al. (2009), and in our work.

The most recent study of the proper motion of Cygnus Loop filaments, based on HST Hα images from three epochs (Blair et al. 1999, 2005, Sankrit et al. 2023), refers to the filament in our FOV *K*. Position of the filament measured by Sankrit et al. (2023) is marked in Fig. 5 as *S*23, and its median derived velocity is 240 km s^{-1}. For this particular

Table 2: Measured filaments, their central coordinates, number of selected pixel rows, proper motion, and speed. The filaments with a name in bold font, given at the end of the table are the ones visible in [SII] images. The measurements J1 and K1 represent the same filament, but observed with different instruments.

Filament	RA [h:m:s]	Dec [d:m:s]	number of rows	p [″]	v [km s^{-1}]
A1	20:53:40.6	32:14:13.2	318	2.3 ± 0.6	310 ± 70
A2	20:53:27.4	32:14:24.0	267	2.0 ± 0.6	280 ± 70
B1	20:54:28.6	32:20:13.2	138	4.0 ± 0.6	550 ± 70
B2	20:54:20.2	32:21:57.6	339	4.7 ± 0.6	650 ± 70
B3	20:54:13.7	32:22:26.4	181	3.6 ± 0.6	490 ± 70
B4	20:54:13.7	32:22:26.4	283	4.2 ± 0.6	580 ± 70
B5	20:54:27.9	32:19:30.0	207	2.0 ± 0.6	270 ± 70
B6	20:54:31.2	32:18:50.4	89	2.8 ± 0.6	380 ± 70
C1	20:54:51.1	32:17:20.4	399	2.5 ± 0.6	350 ± 70
C3	20:54:35.8	32:17:42.0	208	2.1 ± 0.6	290 ± 70
C4	20:54:44.7	32:15:46.8	269	3.5 ± 0.6	480 ± 70
C5	20:54:51.4	32:14:09.6	146	3.2 ± 0.6	440 ± 70
D1	20:54:57.6	32:08:09.6	191	2.5 ± 0.6	340 ± 70
D2	20:55:01.2	32:11:27.6	269	3.2 ± 0.6	440 ± 70
D3	20:55:05.0	32:10:15.6	151	2.2 ± 0.6	300 ± 70
E1	20:55:28.8	32:07:55.2	221	2.7 ± 0.6	370 ± 70
E3	20:55:19.7	32:07:08.4	274	2.1 ± 0.6	280 ± 70
E4	20:55:13.9	32:08:20.4	165	3.0 ± 0.6	400 ± 70
F1	20:55:34.6	32:01:44.4	227	2.1 ± 0.6	280 ± 70
F2	22:55:44.6	31:59:49.2	253	1.9 ± 0.6	260 ± 70
F3	20:55:42.7	32:02:13.2	264	3.3 ± 0.6	460 ± 70
G1	20:55:23.3	32:03:32.4	169	1.8 ± 0.6	240 ± 70
G2	20:55:15.1	32:03:32.4	211	2.3 ± 0.6	310 ± 70
G3	20:55:15.1	32:03:32.4	166	2.0 ± 0.6	280 ± 70
G4	20:55:19.7	32:02:38.4	167	2.0 ± 0.6	280 ± 70
G5	20:55:19.7	32:02:38.4	200	2.1 ± 0.6	290 ± 70
J1	20:55:55.4	31:56:20.4	146	2.4 ± 0.6	310 ± 70
J2	20:55:35.8	32:01:26.4	184	2.6 ± 0.6	340 ± 70
K1	20:55:55.4	31:56:20.4	335	2.5 ± 0.6	330 ± 70
L1	20:53:51.4	32:24:54.0	335	4.4 ± 0.6	580 ± 70
L2	20:53:59.5	32:24:21.6	371	4.3 ± 0.6	570 ± 70
M2	20:53:17.3	32:24:14.4	275	3.6 ± 0.6	470 ± 70
H1	20:55:12.2	31:55:58.8	184	0.9 ± 0.6	130 ± 70
H2	20:54:53.0	31:57:57.6	100	0.7 ± 0.6	100 ± 70
H3	20:54:53.0	31:57:57.6	86	1.1 ± 0.6	160 ± 70

filament, we could not perform proper motion measurement using our method, because the filament $S23$ is not linear.

In Table 3, we list the speed measured in the two mentioned studies (see Salvesen et al. 2009, Medina et al. 2014), for the filaments that are close in position to the ones analyzed in this work. We mark these positions in Figs. 4 and 5. In the case of the study by Medina et al. (2014), the positions marked with red crosses are individual observations obtained before grouping. Within the uncertainty range, most of the speeds obtained in this work are in agreement with the values for nearby filaments from the earlier studies. We note that Salvesen et al. (2009) did not provide any errors, while Medina et al. (2014) presented unrealistically small errors since their shock speed errors reflect only uncertainties in the Hα line profile measurements. This could possibly explain why these studies do not agree with each other for all positions. To this conclusion, we add that these studies used different methods for deriving shock velocities, as well as the fact that our method, like the methods used in Salvesen et al. (2009) and Sankrit et al. (2023) are actually measuring tangential speed, and hence provide a lower limit to the shock speed.

We note that Salvesen et al. (2009) found that in some positions the shock speed was too low to account for the observed X-ray temperatures. This dis-

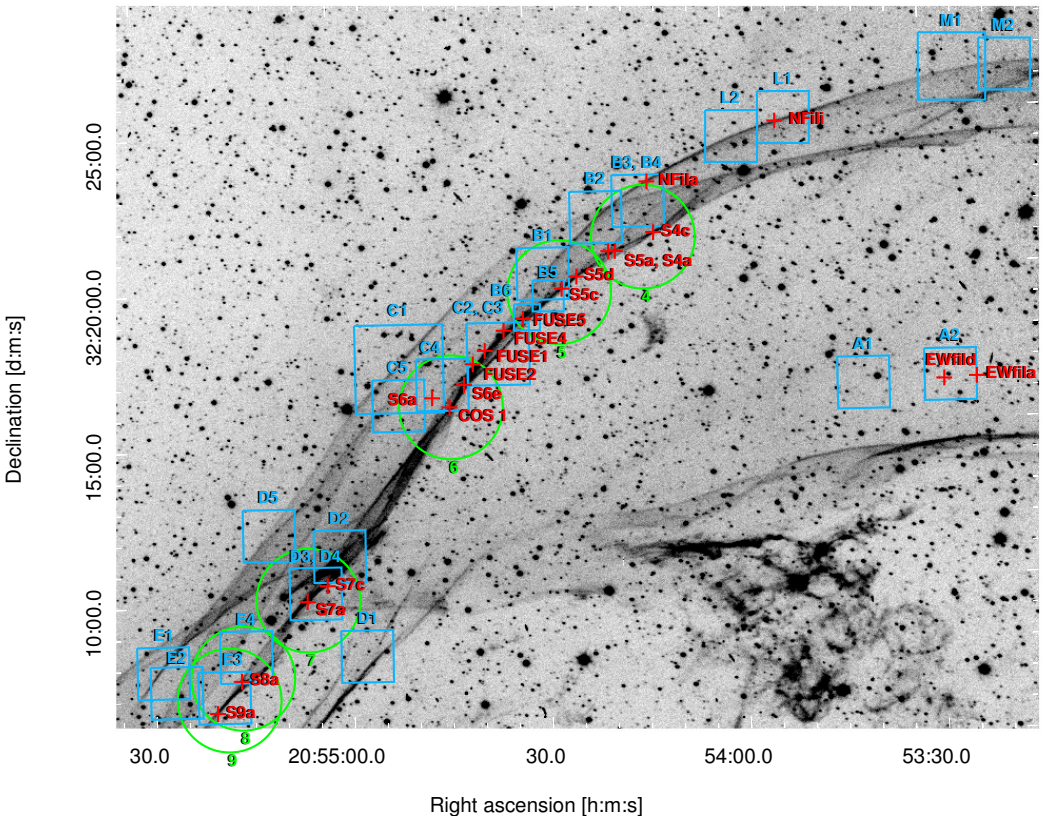

Fig. 4: Comparison between the positions of measured filaments in this work and the earlier studies. The image is located in the northern part of the general region we studied (Fig. 1). The blue squares mark the filaments analyzed in this work. The green circles are the locations analyzed by Salvesen et al. (2009), and the red crosses the ones analyzed by Medina et al. (2014). See Section 4.

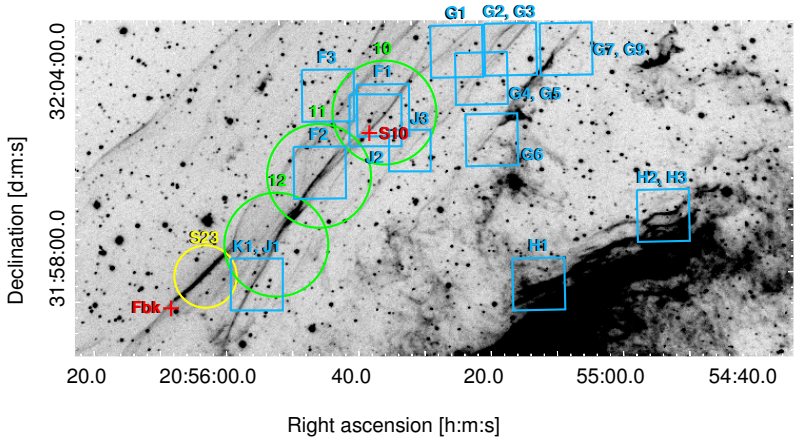

Fig. 5: Comparison between the positions of measured filaments in this work and the earlier studies. The image is located in the southern part of the general region we studied (Fig. 1). The filaments are marked like in Fig. 4, with an additional yellow circle highlighting the location analyzed by Sankrit et al. (2023). See Section 4.

crepancy is partly resolved by using the Fesen et al. (2021) distance to the Cygnus Loop to convert proper motion to shock speed, rather than the smaller 561 ± 61 pc distance used by Salvesen et al. (2009). However, as noted by Medina et al. (2014), the problem still remains for some filaments. In some cases (e.g.,

Table 3: Comparison between the speed of the filaments obtained in this work and the studies by Salvesen et al. (2009) and Medina et al. (2014). The speed is given in km s^{-1}. The speed $v_{\rm S,corr}$ was calculated by adjusting the original speed from their study ($v_{\rm S}$) with the latest value for the remnant's distance (725 ± 15 pc; Fesen et al. 2021).

This work		Salvesen et al. (2009)			Medina et al. (2014)	
Filament	v	Filament	$v_{\rm S}$	$v_{\rm S,corr}$	Filament	$v_{\rm M}$
A2	280 ± 70				EWfil (EWfild)	380 ± 4
B4	580 ± 70				NFil (NFila)	429 ± 22
B5	270 ± 70	5	278	316	S5 (S5c)	376 ± 4
B6	380 ± 70				FUSEB (FUSE5)	414 ± 5
C3	290 ± 70				FUSEB (FUSE4)	414 ± 5
C4	480 ± 70	6	333	379	S6 (S6a), COS 1	391 ± 3, 405 ± 8
D3	300 ± 70	7	240	273	S7 (S7a)	363 ± 5
E3	280 ± 70	9	294	335	S89 (S9a)	457 ± 22, 382 ± 6
F1	280 ± 70	10	279	318	S10	342 ± 46
F2	260 ± 70	11	254	289		
J2	340 ± 70	10	279	318	S10	342 ± 46
L1	580 ± 70				Nfili (Nfil)	429 ± 22

our filament C4) our new proper motion values resolve the problem, but not in all cases. The most likely explanation is that we measure the proper motion of individual sharp filaments, while the measured X-ray temperatures correspond to average values along the line of sight.

5. CONCLUSIONS

We studied the shock speed in the galactic supernova remnant Cygnus Loop, using the narrow-band Hα images from two different epochs. We obtained the speed by measuring the proper motion of the filaments in the remnant, and using the latest estimate for the remnant's distance.

In this work, we analyzed a total of 35 filaments, which is twice as much as in the earlier studies. We estimated their speed, including both non-radiative and radiative filaments. The radiative filaments were selected based on their visibility in [SII] images from the second epoch. Within our sample, there were three radiative filaments.

The speed we obtained for the non-radiative filaments, those filaments that were not detected in [SII] images, is in the range of 240–650 km s^{-1} with the uncertainty of 70 km s^{-1}. These values are mostly in agreement with the earlier studies. The two radiative filaments, which are probably the most well-defined filaments in our sample, have a speed of 100–160 (± 70) km s^{-1}. These values are lower than for the non-radiative filaments and are in agreement with the expected evolution scheme of SNRs. Speeds for the radiative filaments derived in this work are similar to those derived from HST proper motions in the bright western filaments of the Cygnus Loop by Raymond et al. (2020). Our results confirm that the [SII] emission can be used for identification of the radiative phase of the SNR evolution.

Our intention for future work is to obtain radio observations of confirmed radiative and non-radiative filaments in the Cygnus Loop, and search for possible differences in the radio spectral index slopes of these two types of filaments. These steps will enable the study of the particle acceleration processes in different types of shocks.

Acknowledgements – Authors would like to thank anonymous referee for valuable suggestions which improved this paper. Authors also thank prof. Robert A. Fesen from Dartmouth College for sharing his images from year 1993 with us. M.V., D.U., D.O. and S.M. acknowledge funding provided by the University of Belgrade - Faculty of Mathematics (the contract №451-03-47/2023-01/200104) through the grant by the Ministry of Science, Technological Development and Innovation of the Republic of Serbia. M.V., D.U., N.P., D.O. and S.M. also acknowledge the observing and financial grant support from the Institute of Astronomy and NAO Rozhen through the bilateral joint research project between the Bulgarian Academy of Sciences and Serbian Academy of Sciences and Arts. The authors acknowledge the support by the Astronomical Station Vidojevica and funding from the Ministry of Science, Technological Development and Innovation of the Republic of Serbia, Contract No. 451-03-47/2023-01/200002 and by the EC through the Project BELISSIMA (call FP7-REGPOT-2010-5, No. 265772).

REFERENCES

Blair, W. P., Sankrit, R., Raymond, J. C. and Long, K. S. 1999, AJ, 118, 942

Blair, W. P., Sankrit, R. and Raymond, J. C. 2005, AJ, 129, 2268

Chevalier, R. A., Kirshner, R. P. and Raymond, J. C. 1980, ApJ, 235, 186

Fesen, R. A., Neustadt, J. M. M., Black, C. S. and Milisavljevic, D. 2018a, MNRAS, 475, 3996

Fesen, R. A., Weil, K. E., Cisneros, I. A., Blair, W. P. and Raymond, J. C. 2018b, MNRAS, 481, 1786

Fesen, R. A., Weil, K. E., Cisneros, I., Blair, W. P. and Raymond, J. C. 2021, MNRAS, 507, 244

Ghavamian, P., Raymond, J., Smith, R. C. and Hartigan, P. 2001, ApJ, 547, 995

Hester, J. J. and Cox, D. P. 1986, ApJ, 300, 675

Hester, J. J., Raymond, J. C. and Blair, W. P. 1994, ApJ, 420, 721

Lang, D., Hogg, D. W., Mierle, K., Blanton, M. and Roweis, S. 2010, AJ, 139, 1782

Matonick, D. M. and Fesen, R. A. 1997, ApJS, 112, 49

Medina, A. A., Raymond, J. C., Edgar, R. J., et al. 2014, ApJ, 791, 30

Milanovic, N., Vucetic, M., Onic, D., Raymond, J. and Urosevic, D. 2019, in Supernova Remnants: An Odyssey in Space after Stellar Death II, 127

Minkowski, R. 1958, RvMP, 30, 1048

Raymond, J. C. 1979, ApJS, 39, 1

Raymond, J. C., Slavin, J. D., Blair, W. P., et al. 2020, ApJ, 903, 2

Raymond, J. C., Ghavamian, P., Bohdan, A., et al. 2023, ApJ, 949, 50

Salvesen, G., Raymond, J. C. and Edgar, R. J. 2009, ApJ, 702, 327

Sankrit, R., Blair, W. P. and Raymond, J. C. 2023, ApJ, 948, 97

Vučetić, M. M., Ćiprijanović, A., Pavlović, M. Z., et al. 2015, SerAJ, 191, 67

СОПСТВЕНО КРЕТАЊЕ ФИЛАМЕНАТА У ОСТАТКУ СУПЕРНОВЕ ЛАБУДОВА ПЕТЉА

М. Вучетић[1], Н. Милановић[2], Д. Урошевић[1], J. Raymond[3], Д. Онић[1], С. Милошевић[1] and N. Petrov[4]

[1]*Катедра за астрономију, Математички факултет, Универзитет у Београду, Студентски трг 16, 11000 Београд, Србија*

E–mail: *milica.vucetic@matf.bg.ac.rs*

[2]*Max Planck Institute for Solar System Research, Justus-von-Liebig-Weg 3, 37077 Göttingen, Germany*

[3]*Harvard-Smithsonian Center for Astrophysics, 60 Garden Street, Cambridge, MA, 02138, USA*

[4]*Institute of Astronomy and National Astronomical Observatory, Bulgarian Academy of Sciences, Tsarigradsko Shose 72, BG-1784 Sofia, Bulgaria*

УДК 524.354–75
Оригинални научни рад

У овом раду одређене су брзине ударног таласа у Галактичком остатку супернове Лабудова петља, мерећи сопствена кретања њених оптичких филамената. Сопствена кретања су одређена поређењем Hα снимака остатка у две епохе. Прва епоха је била 1993. године (KPNO), а друга 2018. и 2019. године (Национална астрономска опсерваторија Рожен, Астрономска станица Видојевица). Одредили смо брзине удара за 35 позиција дуж различитих филамената, што је двоструко више него у претходним студијама везаним за овај део Лабудове петље. По први пут, измерили смо брзине радијативних филамената у овом региону. Међу проучаваним филаментима налазе се три мерења која долазе са два радијативна филамента, која су одабрана на основу тога што су ти филаменти видљиви на [SII] снимцима из друге епохе. Брзине добијене за нерадијативне филаменте су у опсегу 240–650 km s^{-1} са грешком од 70 km s^{-1} што је у сагласности са претходним студијама. Два радијативна филамента имају знатно ниже брзине од 100–160 ± 70 km s^{-1}, што је у сагласности са претпоставком да су ти филаменти еволутивно старији. Ово доказује да се емисија у [SII] линији може користити за одабир радијативних филамената у остацима супернових.